ACS Energy LETTERS

http://pubs.acs.org/journal/aelccp

Operando Raman and DFT Analysis of (De)lithiation in Fast-Charging, Shear-Phase H-Nb_2O_5

Tongtong Li, Shengchi Huang, Nicholas Kane, Jeng-Han Wang,* Zheyu Luo, Weilin Zhang, Gyutae Nam, Bote Zhao, Yabing Qi,* and Meilin Liu*

Cite This: *ACS Energy Lett.* 2023, 8, 3131−3140

Read Online

ACCESS | Metrics & More | Article Recommendations | Supporting Information

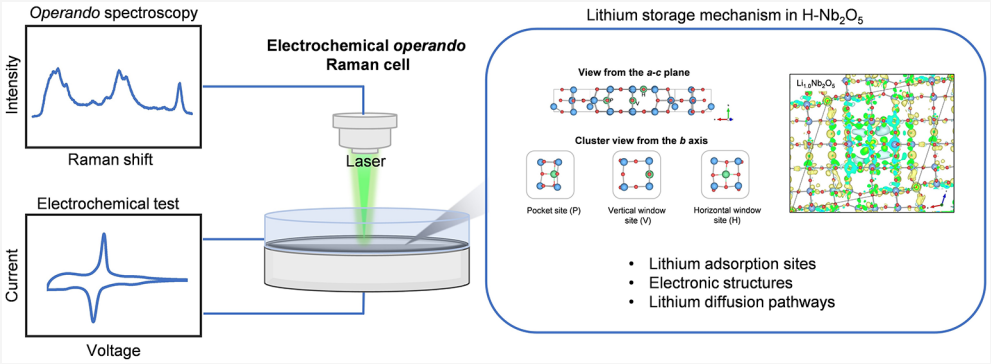

ABSTRACT: **Niobium-based compounds with Wadsley−Roth crystallographic shear structures show promise as fast lithium storage materials in micrometer sizes without the need for nanostructure engineering. However, the lithium storage mechanism underlying their unique electrochemical properties has yet to be understood. Herein, we characterized the evolution of vibration bands in *operando* Raman spectra of the representative shear phase, H-Nb_2O_5, during lithiation in order to correlate the lithiation-induced structural variations of H-Nb_2O_5 with the electrochemical properties. Complemented by DFT calculations, the lithium storage mechanism was unraveled, including the preference for adsorption sites, the resultant electronic structure, and specific pathways for lithium transport. This work provides insight into the lithium storage mechanism in shear structure Nb_2O_5, which is believed to be useful for knowledge-based design of niobium-based compounds as high-rate lithium storage materials.**

Lithium-ion batteries (LIBs) with high power density could shorten the charge time, which can alleviate consumers' "charge anxiety" and improve user experience in electric vehicles, electronic devices, and household appliances. The charge rate of LIBs depends sensitively on the ionic and electronic conductivity of the electrode materials. The ionic conductivities of the active electrode materials are often much smaller than the electronic conductivities.[1] The lithium diffusivities (D) of electrode materials are generally much smaller than those of the electrolyte materials (liquid or solid).[2] Thus, one common strategy to compensate for the slow lithium diffusion when designing a fast-charging electrode is to shorten the diffusion length (L) by reducing the particle size of the material, thus reducing the time ($\tau = L^2/D$) required for full lithiation.[3,4] However, this approach may degrade the cycling stability, capacity retention, and volumetric energy density of the electrodes; further, the preparation of nanomaterials may involve expensive, toxic, and complex preparation processes.[4] If the electrode material has an intrinsically high Li-ion diffusivity, the use of nanomaterials can be avoided.

Many niobium-based oxides with an open-frame crystal structure, a so-called shear structure, such as $TiNb_2O_7$,[5,6] $Nb_{16}W_5O_{55}$, $Nb_{18}W_{16}O_{93}$,[7] etc., exhibit rapid Li-ion diffusion.

Received: May 25, 2023
Accepted: June 20, 2023
Published: June 23, 2023

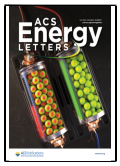

https://doi.org/10.1021/acsenergylett.3c01031
ACS Energy Lett. 2023, 8, 3131−3140

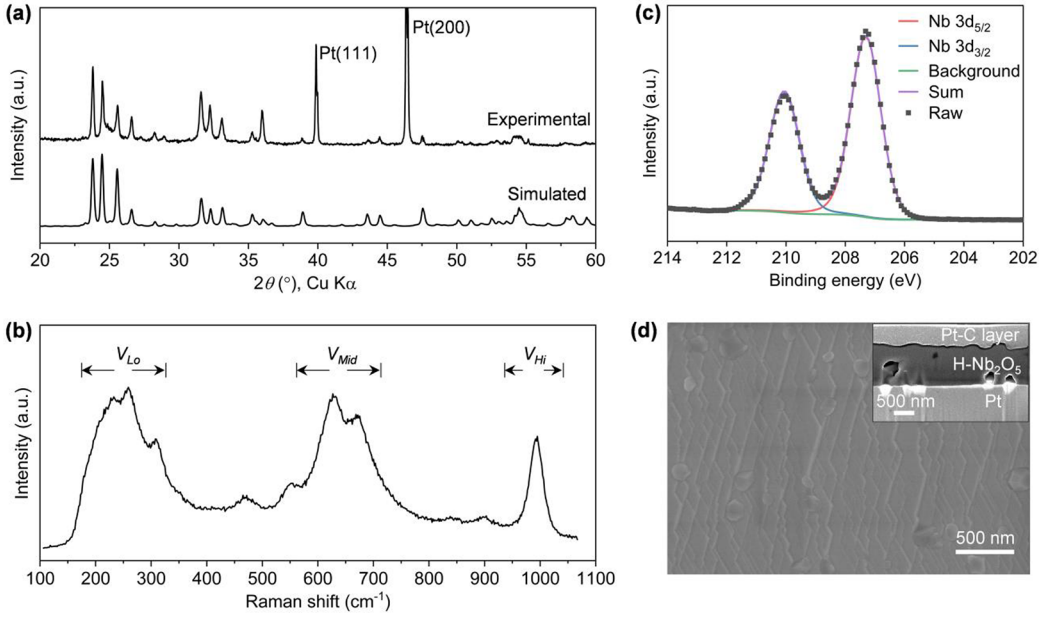

Figure 1. (a) XRD pattern, (b) Raman spectrum, (c) XPS spectrum, and (d) SEM image of the as-prepared H-Nb_2O_5 thin film. The inset in (d) shows a cross-sectional image of the H-Nb_2O_5 thin film.

In other words, these shear-phase materials can achieve fast lithium storage without being nanosized and enable high volumetric energy and power density without compromising the rate capability. Unraveling the lithium storage mechanism of the shear phase is especially important for the design of a new generation of storage materials with high power densities. To date, various state-of-the-art characterization techniques have been applied to explore their unique Li-ion storage properties. For example, Lu et al. revealed that Li-ion sites are possibly located in the (001) lattice plane of $TiNb_2O_7$ by using first-principles calculations and spherical aberration-corrected scanning transmission electron microscopy.[8] Catti et al. and Saber et al. investigated the lithium site preference and electronic properties in $Li_{1.714}Nb_2O_5$ and PNb_9O_{25}, respectively, with the aid of neutron powder diffraction and first-principles calculations.[9,10] Furthermore, Griffith et al. demonstrated using structural analysis and bond valence summation (BVS) that Li ions in $Nb_{16}W_5O_{55}$ diffuse one-dimensionally along the tunnels formed by the shear plane and change the migration path through local hopping between the tunnels, where the lithium sites and diffusion may be analogous to those in the ReO_3 and lanthanum lithium titanate (LLTO) structure.[7] Nevertheless, the current research regarding the Li-ion intercalation mechanism in shear structure materials is still in the preliminary stage. Unraveling the intercalation mechanism is challenging due to the structural complexity of the shear phases. On one hand, the ternary Nb system (Ti-Nb-O/Nb-W-O) with different transition metals may have distinct lithium diffusion path topologies due to various cation configurations. Even the diversity and uncertainty of local cation ordering might have a significant effect on the lithium storage and transport.[11] On the other hand, due to the diverse range of dopants and defects in the shear structure family, understanding the process of lithium intercalation becomes more intricate, as there are myriad materials to consider.[6]

While the atomic structures of the shear compounds are complex, they hold close crystallographic structural relationships to the high-temperature phase of Nb_2O_5 (H-Nb_2O_5).[12] Their common features include ReO_3-like $n \times m$ corner-sharing octahedral building blocks, shear planes formed by the edge-sharing octahedra linking these blocks, and possible voids in the corners filled by tetrahedra.[13] Therefore, understanding the lithium storage behavior in H-Nb_2O_5 is crucial for providing a comprehensive picture of the characteristic diffusion mechanism in other shear structures. Compared with common characterization technologies, Raman spectroscopy is a highly effective tool for probing the dynamic behavior of interacting molecules on a surface or for obtaining structural information on a crystal under stimulation.[14−20] By combining vibrational analysis, Raman spectroscopy has proven to be successful in interpreting the structural properties of energy storage and conversion materials.[21−24] Nonetheless, unlike some energy materials crystallized at low temperatures, the shear phases formed at high temperatures give a large crystal with uncontrolled geometry, which is not advantageous for achieving efficient Raman spectroscopic acquisitions. The related *operando* Raman study is extremely rare.

In this study, a thin film of H-Nb_2O_5 was prepared by using radio frequency (RF) magnetron sputtering, followed by heat treatment. The vibrational modes of H-Nb_2O_5 during lithiation/delithiation were analyzed by using *operando* Raman spectroscopy. Density functional theory (DFT) calculations were performed to complement the experimental results and explain the vibration modes, predict the adsorption energy of lithium on different sites, and determine the diffusion energy barriers between them. Our findings provide a detailed explanation of the lithiation mechanism in H-Nb_2O_5, highlighting the preference of lithium ions for specific sites, the corresponding electronic structure, and lithium transport pathways during the process. The discovery of the interplay between lithium and H-Nb_2O_5 presented in this study is essential for understanding the energy storage mechanism and fast-charging properties of shear phase materials.

The sputtered Nb_2O_5 thin film shows different phases depending on the temperature of the heat treatment (Figures S1 and S2). Two obvious peaks at $2\theta \approx 40$ and 47° in their

https://doi.org/10.1021/acsenergylett.3c01031
ACS Energy Lett. 2023, 8, 3131−3140

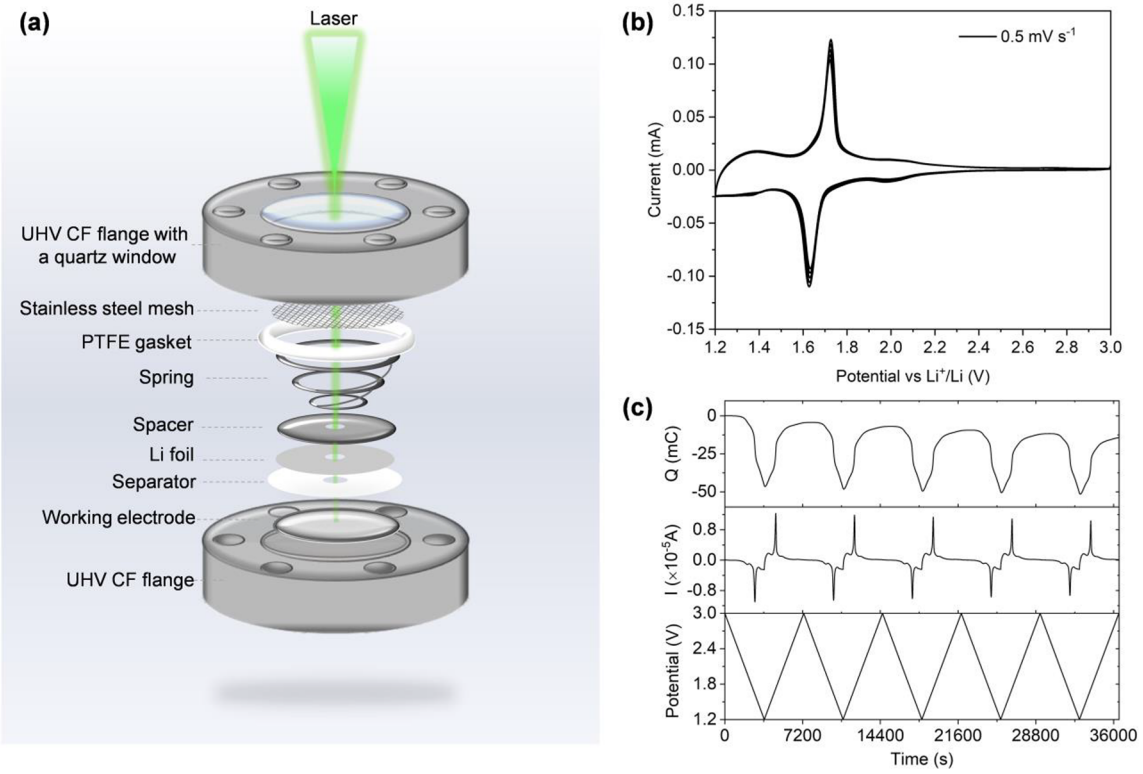

Figure 2. (a) Schematic illustration of the model cell used for the *operando* Raman study. (b) Cyclic voltammogram (CV) of the H-Nb_2O_5 thin film at a sweep rate of 0.5 mV s^{-1} for five cycles acquired in the model cell. (c) Applied potential, collected current, and quantity of stored charge of the H-Nb_2O_5 thin film as a function of the scanning time.

diffraction pattern belong to the (111) and (200) crystal planes of the Pt substrate, respectively. Apart from that, the XRD pattern of the thin film obtained after annealing above 1000 °C matches well with the characteristic peak of the monoclinic Nb_2O_5 (PDF 01-072-1121)[25] (Figure 1a and supplementary note 1). In addition, there are no peaks indexed to Pt oxides or PtNb alloys, which proves the successful preparation of H-Nb_2O_5 thin films on the substrate. Figure 1b shows the typical Raman spectrum of the H-Nb_2O_5 thin film. The position and profile of the vibration bands are consistent with those of the H-Nb_2O_5 powder.[26] For the convenience of the subsequent discussion, these vibration bands are divided into three parts from low to high wavenumbers, including V_{Lo} (200−350 cm^{-1}), V_{Mid} (600−700 cm^{-1}), and V_{Hi} (∼1000 cm^{-1}). According to the vibration analysis detailed below, the V_{Lo} band corresponds to the bending mode of the O−Nb−O bond, while the V_{Mid} and V_{Hi} bands correspond to the stretching modes of the Nb−O bond. Typical spin−orbit doublets at 210.0 and 207.3 eV in the Nb 3d XPS spectra for the H-Nb_2O_5 thin film confirm that the Nb atoms are in the +5 valence state (Figure 1c). The SEM images of the as-sputtered Nb_2O_5 thin film reveal a uniform surface but with numerous small crevices (as seen in Figure S3). Upon heating, these crevices vanish as the grains increase in size, leading to a relatively smooth H-Nb_2O_5 thin film with a thickness of approximately 1 μm, as shown in Figure 1d and Figure S3. This is crucial for obtaining a robust signal for the *operando* Raman study.

Figure 2a shows the schematic illustration of the model cell used for the electrochemical tests and *operando* Raman study, which is assembled by sequentially stacking the H-Nb_2O_5 thin film (working electrode) and the other cell components. The CV curves acquired in the model cell show obvious redox peaks at ∼1.7 V, representing a typical two-phase process of H-Nb_2O_5 upon (de)lithiation (Figure 2b). A solid solution reaction at the beginning and near the end of the charging/discharging processes contributed to the partial capacity as well. The overlapped redox peaks and CV profiles upon continuous scans indicate the good reversibility of the electrode material and the reliability of the model cell. This is also verified by the good periodicity of the corresponding stored charge versus scan time (Figure 2c). Though a slightly decreased Coulombic efficiency is shown, it is tolerable for an *operando* Raman study considering that no conductive agent and binder were added for the thin-film electrode (mass loading ∼0.5 mg cm^{-2}). Furthermore, no obvious separation of the redox peaks at a scan rate of 0.5 mV s^{-1} suggests good reaction kinetics of the electrode as well.

The Raman spectra of the Pt substrate and the electrolyte were investigated before Raman characterization of H-Nb_2O_5. The results in Figure S4 show that metallic Pt has no Raman-active vibration band before or after calcination. Due to the coexistence of three different organic compounds and the solvation effect, the Raman spectrum of the commercial electrolyte is complex (details in Figure S4). The two strongest Raman bands of the electrolyte at ∼720 and ∼900 cm^{-1} are attributed to the overlapped signals of EC/PF_6^- and EC/DMC, respectively.[23] The other two bands at 518 and 973 cm^{-1} belong to the DMC and EC signals, which are too weak to be found in the subsequent *operando* studies.

In the 2D contour plot, the *operando* Raman spectra (Figure 3a) near each cycle number correspond to states at a high potential, and those between two cycle numbers represent states at a low potential. In the pristine states, the three red

https://doi.org/10.1021/acsenergylett.3c01031
ACS Energy Lett. 2023, 8, 3131−3140

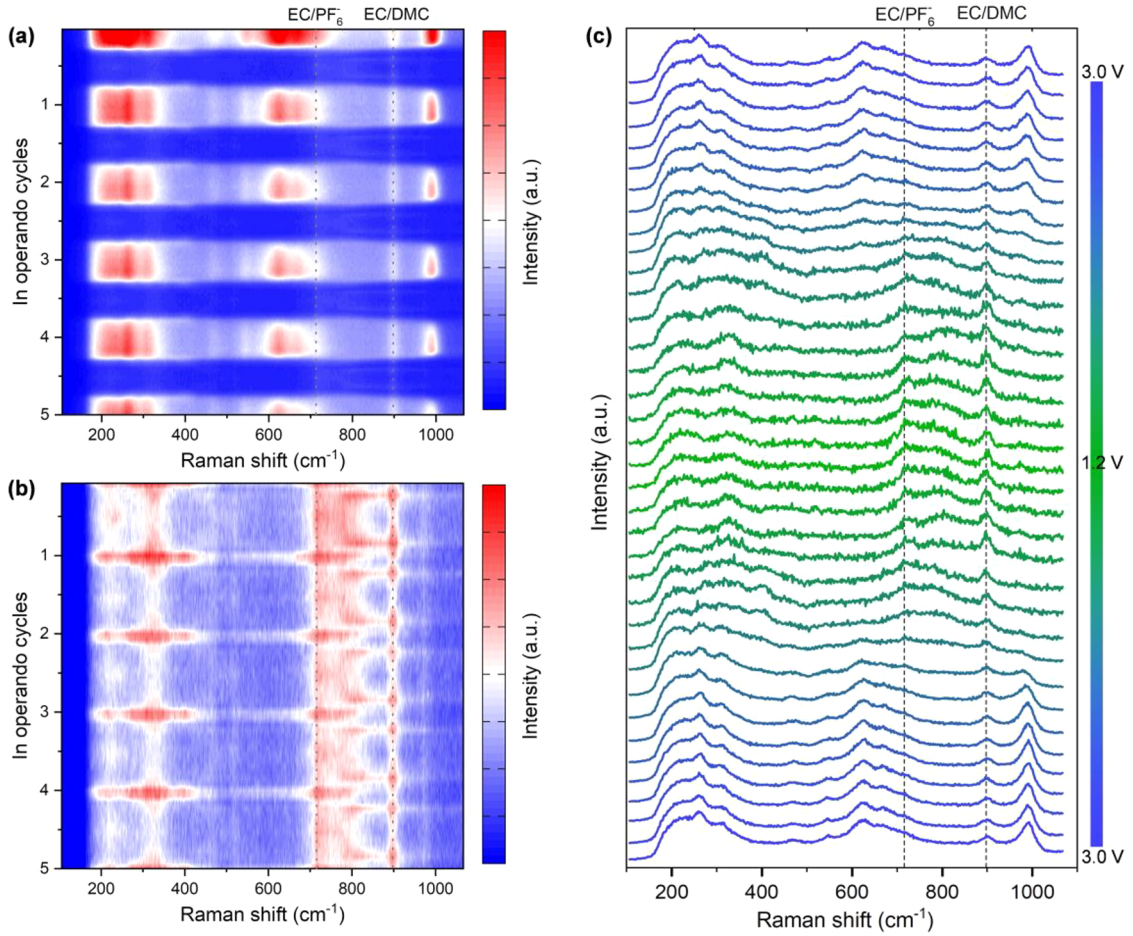

Figure 3. 2D contour plots showing the Raman spectra of the structural evolution of H-Nb_2O_5 as the potential varied (a) from 3.0 to 1.2 V and (b) from 1.8 to 1.2 V extracted from (a) for 5 cycles. (c) Stacked Raman spectra of H-Nb_2O_5 in one cycle of lithiation/delithiation. The gray dashed lines in (a)−(c) correspond to the band position of the electrolyte.

zones of the contour map correspond to the V_{Lo}, V_{Mid}, and V_{Hi} bands, which have a higher Raman intensity. Figure 3 and Figure S5 show that the band intensities of H-Nb_2O_5 change periodically during electrochemical cycling and the evolution of the Raman spectrum is completely reversible. More specifically, the intensities of three representative bands show periodic decreases or increases when lithium ions are intercalated into or extracted from the materials. The abrupt decrease in the Raman signal could be explained by the significant enhancement of the electrical conductivity of H-Nb_2O_5 upon initial lithiation. This conductivity change suggests that $Li_xNb_2O_5$ becomes a semiconductor or even a conductor from a pristine insulator with increasing lithium composition. Due to the decrease of the overall Raman signal, specific band changes, such as peak splitting and shifting at the low potential range, cannot be distinguished in the same scale. To this end, the Raman signals in the intervals between 1.8 and 1.2 V are replotted in the same manner, as shown in Figure 3b. The Raman signals around 720 and 900 cm^{-1} correspond to the bands of EC/PF_6^- and EC/DMC in the electrolyte, respectively. In a subsequent analysis, these peaks are used as the reference to observe the changes in the Raman spectra. Figure 3b shows that the pristine V_{Mid} (600−700 cm^{-1}) and V_{Hi} bands (~1000 cm^{-1}) vanish, while a new band appears between them at 800 cm^{-1} in the Raman spectrum of H-Nb_2O_5 in the low-voltage range. At low wavenumbers, the original V_{Lo} (200−350 cm^{-1}) band gradually weakens, and two new bands at higher wavenumbers (330 and 400 cm^{-1}) appear when lithium intercalates. The above spectroscopic changes during discharge are reversed during the charge process. In addition, the evolution of the Raman spectrum of H-Nb_2O_5 within one cycle demonstrates these changes more clearly (Figure 3c). The spectra show that the signal of the electrolyte is covered by the stronger Raman signal of Nb_2O_5 when the voltage is 3.0 V: that is, when lithium ions are not intercalated into the structure. As the voltage gradually decreases, the intensities of the V_{Mid} and V_{Hi} bands become weaker. The V_{Hi} band first vanishes when the cell is discharged to ~2.0 V, and the V_{Mid} band disappears subsequently. In the meantime, lithium insertion debilitates the V_{Lo} band, and the peaks in the V_{Lo} region gradually emerge and shift to higher wavenumbers. Overall, compared with the pristine H-Nb_2O_5 spectrum, fully lithiated H-Nb_2O_5 exhibits a new band at approximately 800 cm^{-1}. The V_{Mid} and V_{Hi} bands are no longer present, and the V_{Lo} band experiences positive shifts. During charging, the Raman signal of H-Nb_2O_5 reverses the above processes, and finally, the spectrum returns to its initial state at 3.0 V.

To investigate the effect of the structural variation caused by the lithium insertion on the Raman spectra, the contribution of evolutions in electronic structures and vibrations was analyzed through DFT calculations as detailed in the following text. First, the structures and energies of Li adsorption at the oxygen

https://doi.org/10.1021/acsenergylett.3c01031
ACS Energy Lett. 2023, 8, 3131−3140

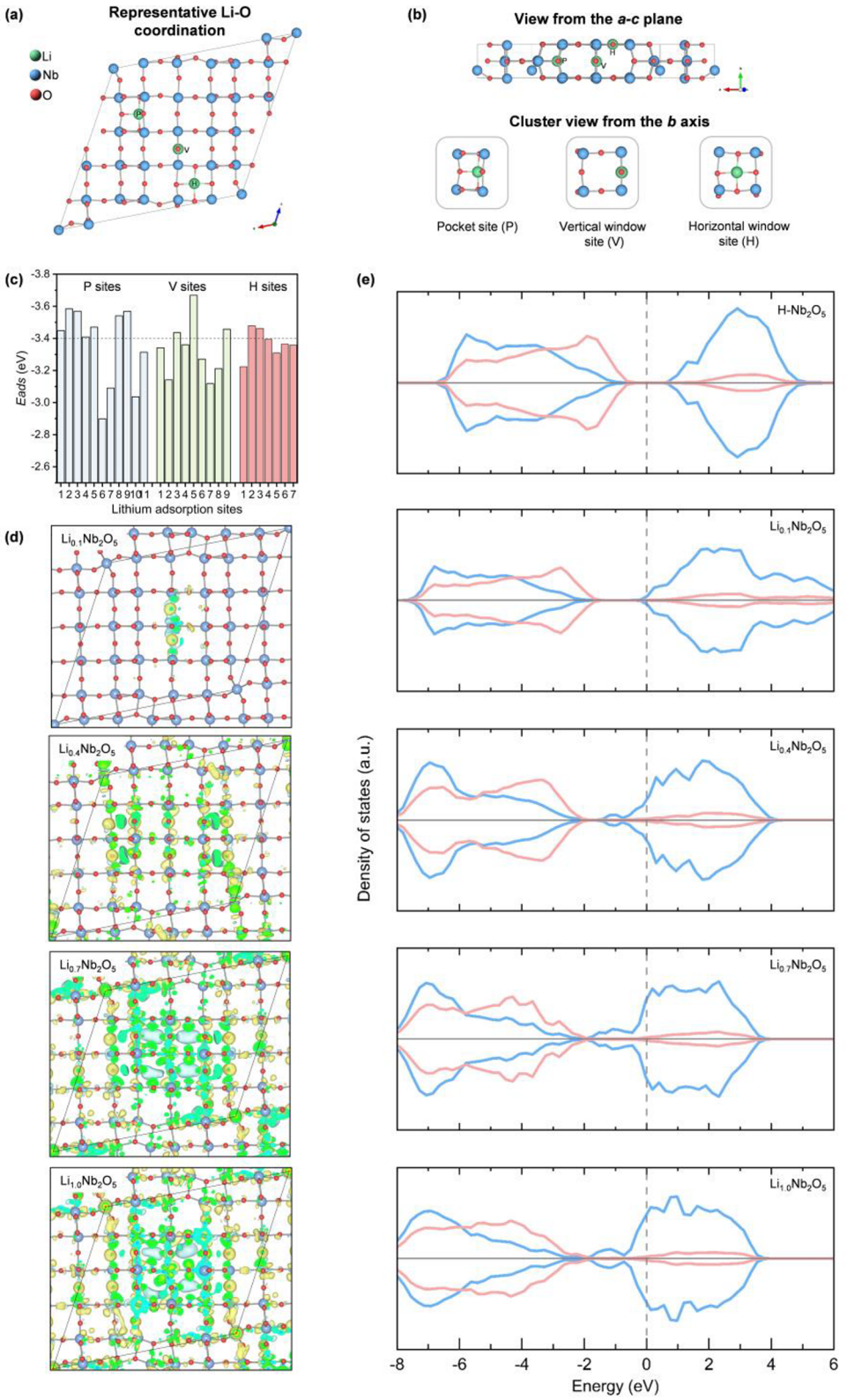

Figure 4. (a) View of three types of Li adsorption sites in H-Nb_2O_5 from the *b* axis. (b) View from the *a*−*c* plane and cluster view from the *b* axis. (c) Related adsorption energy (E_{ads}) of the distinct Li adsorption sites, detailed in Figure S7, in H-Nb_2O_5. (d) Charge density analysis of Li-adsorbed H-Nb_2O_5. The yellow and cyan colors represent positive and negative charge densities, respectively. (e) DOS analysis of pristine and Li-adsorbed H-Nb_2O_5. The valence Nb d bands and O p bands are plotted as blue and red lines, respectively.

sites in H-Nb_2O_5 were examined. H-Nb_2O_5 crystallizes in the monoclinic *P*2 space group and adopts a shear structure with staggered 3 × 4 and 3 × 5 corner-sharing NbO_6 blocks, as shown in Figure 4a and Figure S6.[25] These two kinds of blocks are connected to each other by the NbO_4 tetrahedra and the edge-sharing NbO_6, in which the latter produces a structure

https://doi.org/10.1021/acsenergylett.3c01031
ACS Energy Lett. 2023, 8, 3131−3140

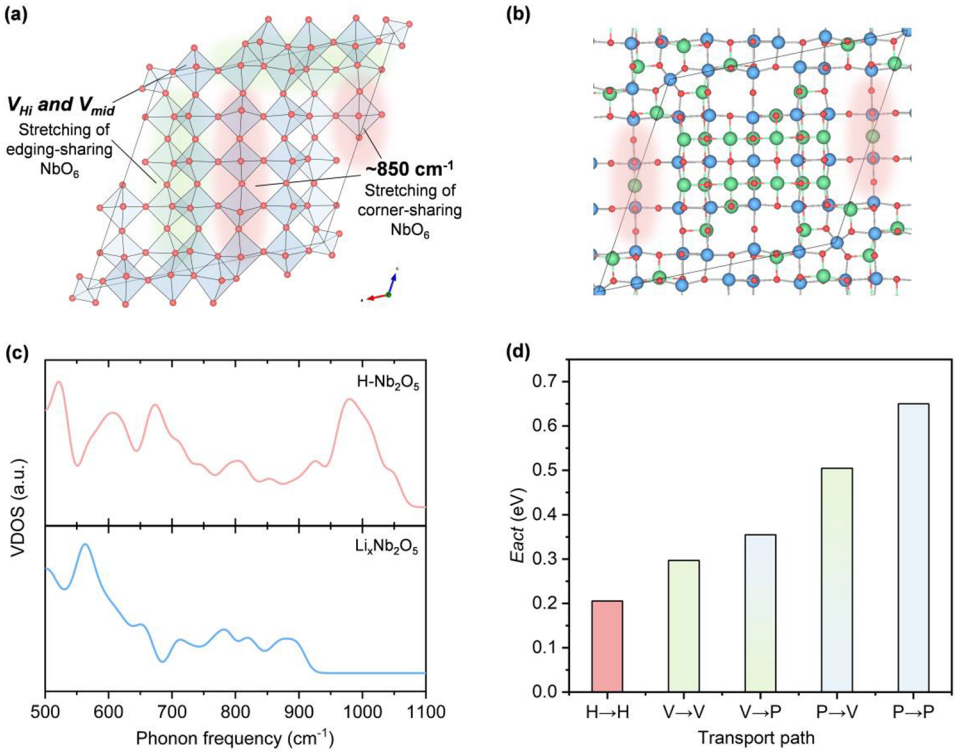

Figure 5. (a) Polyhedral model of the crystal structure of H-Nb_2O_5 visualized from the *b* axis. (b) Li adsorption sites with higher E_{ads} (<−3.4 eV), $Li_{1.0}Nb_2O_5$. The Nb−O stretching mode shaded red in 3 × 4 corner-sharing blocks is assigned to the peaks around 800 cm^{-1} at low voltage. (c) Vibrational density of state (VDOS) of pristine H-Nb_2O_5 and $Li_{1.0}Nb_2O_5$ estimated from the force constants in the vibrational calculation. (d) Average E_{act} of Li diffusion through different steps of H → H, V → V, V → P, P → V and P → P; details of each step are shown in Figure S9.

motif named a shear plane. As shown in Figure 4a,b, the adsorption in H-Nb_2O_5 can be divided into two categories according to the number of Li−O bonds: the square-planar site, or so-called "window site" (Li coordinated by four O) in the corner-sharing blocks, and the square-pyramidal site, or so-called "pocket sites" (Li coordinated by five O), in the edge-sharing blocks.[9,11,27] Additionally, the window site includes both vertical and horizontal Li-O bonds, in which Li-O bonds are in the *ac* plane and along the *b* axis, respectively. These sites have been thoroughly examined for their Li adsorption energy (E_{ads}) in the present work (Figure 4c and Figure S7 and Table S1). Pocket sites with five Li−O bonds are expected to have a stronger E_{ads}, whereas both horizontal and vertical window sites have a weaker E_{ads} due to the fewer number of Li−O bonds (four).[10,11] The energy analysis finds two conclusive trends. First, most of the pocket sites have stronger E_{ads} (<−3.40 eV) than horizontal and vertical window sites. Second, the window sites, closer to the center in the corner-sharing blocks, have stronger E_{ads}; the strongest sites are located at the center of the 3 × 5 corner-sharing blocks.

Figure 4d shows the charge density of Li-adsorbed H-Nb_2O_5 with stronger E_{ads} (<−3.40 eV). Lithium was gradually added into pristine H-Nb_2O_5 according to their adsorption energy, forming $Li_{0.1}Nb_2O_5$, $Li_{0.4}Nb_2O_5$, $Li_{0.7}Nb_2O_5$, and $Li_{1.0}Nb_2O_5$ for E_{ads} < −3.60, −3.50, −3.45, and −3.40 eV, respectively. When Li initially adsorbs in H-Nb_2O_5 (e.g., $Li_{0.1}Nb_2O_5$), the introduced electron localizes in the empty Nb d orbital of NbO_6 octahedra at the center of the 3 × 5 blocks. Specifically, the electron preferentially fills the Nb d_{xy}, d_{yz}, and d_{zx} orbitals, which are the lower energy t_{2g} and the nonbonding orbitals in NbO_6 octahedra.[10,28] As more Li adsorbs in H-Nb_2O_5, additional electrons begin to occupy the lower energy t_{2g} orbitals of the edge-sharing octahedra with shorter metal−metal distances, resulting in enhanced d orbital overlap. Consequently, the charge distribution becomes more delocalized, indicating an increased conductivity. The increased conductivity of $Li_xNb_2O_5$ is also evident in the DOS plots (Figure 4e). In pristine H-Nb_2O_5, the valence Nb d band contributes to the conduction band at higher energy, while the p band contributes to the valence band at lower energy. The DOS analysis reveals a large band gap, as the Nb d band has a considerably high energy, well above the Fermi level, and the O p band has a low energy. Furthermore, the high-energy Nb d band indicates its empty d orbitals, corresponding to its 5+ formal oxidation state. When Li adsorbs and forms $Li_xNb_2O_5$, the electrons are introduced into the empty conduction band, which lowers the energy of the DOS. As electrons mostly fill the empty Nb d orbitals, the Nb d band experiences an energetic drop and reduced band gap. As shown in the DOS plot, $Li_{0.7}Nb_2O_5$ has become conductive, with a negligible band gap. This insulator-to-metal transition behavior upon lithiation is also manifested in the optical color change, progressing from white to blue and eventually to a dark black hue in a series of lithiated niobium-based oxides.[26,28] Although changes in material polarizability upon lithiation and thermal effects caused by the high-power laser might also contribute to Raman intensity changes, the abrupt drop in overall Raman signal of $Li_xNb_2O_5$ could be mainly attributed to the delocalized electron configuration (i.e., improved electronic conductivity) that significantly decreases the incident photon frequency (ω) through the Compton effect, as the intensity is proportional to ω^4 (see supplementary note 2).

https://doi.org/10.1021/acsenergylett.3c01031
ACS Energy Lett. 2023, 8, 3131−3140

Besides the overall intensity, changes in the Raman profile can provide structural information regarding the incorporation of lithium. The assignment of the Raman spectra was initially carried out through structrual analysis, and subsequently, DFT calculations were employed to validate the assignments and lithium-induced variation by examining the vibrational density of states (VDOS) (supplementary note 3). In the crystal structure of H-Nb_2O_5, the NbO_6 octahedra are distorted to some extent due to the ionic repulsion and Jahn−Teller effect, as shown in Figure 5a.[11] The Nb−O bond distances are in the range of 1.8−2.3 Å. The octahedra along the shear planes in edge-sharing blocks show stronger distortion than those in the center of corner-sharing blocks, which induces shorter Nb−O bond distances (<1.9 Å, numbered in Figure S8) and higher vibrational freqnencies. Accordingly, the highest frequency of V_{Hi} in the *operando* Raman spectrum corresponds to stretching modes of those shorter Nb−O bonds around the edge-sharing octahedra, as assigned in Figure 5a (vertical green shading) and detailed in Supporting Video a. V_{Mid} is also assigned to stretchings in edge-sharing octahedra (horizontal green shading and Supporting Video b). Those vibrations have a strong Raman intensity, attributed to the structural rigidity of the edge-sharing blocks.[29] On the other hand, the vibrations in corner-sharing octahedra have a weaker Raman intensity with a frequency around 850 cm^{-1} (red shading and Supporting Video c).[30] V_{Lo} in the Raman spectrum is related to the bending modes (e.g., rocking and wagging).[31] Due to the perturbation between neighboring octahedra, those modes are rather complicated and do not solely correspond to one specific vibration, and some examples are shown in Supporting Video d.

Figure 5b demonstrates Li adsorbed on the sites with stronger E_{ads} (<−3.4 eV), $Li_{1.0}Nb_2O_5$. A stronger E_{ads} implies more stable Li adsorption; thus, the pocket- and center-corner-sharing sites are expected to be firmly occupied by Li during lithiation at lower voltages. As a result, the strict Li adsorptions in the pocket sites hinder the vibrations in the edge-sharing octahedra and thus are responsible for the disappearance of the V_{Hi} and V_{Mid} bands in the Raman spectra during lithiation at low voltages (Figure 3c). On the other hand, the vibrations in the corner-sharing octahedra, shaded red in Figure 5b and detailed in Supporting Video e, are less ruined during lithiation and are still observable in the Raman spectra (at ∼800 cm^{-1}) at low voltages (1.8−1.2 V). We further utilized the force constants derived from vibrational calculations to examine VDOS of pristine H-Nb_2O_5 and $Li_{1.0}Nb_2O_5$ (Figure 5b) and compared them with the *operando* Raman spectra obtained at high and low potentials, corresponding to delithiated and lithiated H-Nb_2O_5, respectively. The computed VDOS of pristine H-Nb_2O_5 and $Li_{1.0}Nb_2O_5$ is presented in Figure 5c. Due to the complicated coupling of bending modes, the VDOS at low frequencies (<500 cm^{-1}) is challenging to analyze and thus not shown. Significant differences are observed between the two VDOS in the high-frequency region of 900−1100 cm^{-1}. The VDOS for pristine H-Nb_2O_5 exhibits a distinct distribution, while that for $Li_{1.0}Nb_2O_5$ appears flat in this region. This high-frequency distribution corresponds to the Nb−O stretching vibrations associated with shorter bond lengths in the edge-sharing octahedra of pristine H-Nb_2O_5. Furthermore, the VDOS of $Li_{1.0}Nb_2O_5$ displays a small bump in the range of 700−900 cm^{-1}, which is attributed to the Nb−O stretching in the corner-sharing octahedra. The VDOS analysis yields results that closely resemble the *operando* Raman spectra, where pristine H-Nb_2O_5 exhibits strong Raman intensity at high frequency (V_{Hi}), which disappears at low potential in lithiated H-Nb_2O_5. Instead, a new band emerges at around 800 cm^{-1}. The explanation regarding Raman band variation upon lithium insertion could also be understood by the distortion of NbO_6 octahedra in the H-Nb_2O_5 crystal. Lithium intercalation will increase the local octahedral symmetry of Nb_2O_5 due to the alleviation of the second-order Jahn−Teller distortion.[26] At the same time, this symmetrization makes previously distorted NbO_6 available for lithium occupation.[11] As previously mentioned, NbO_6 octahedra at edge sites corresponding to the V_{Hi} and V_{Mid} bands are more distorted than those at the center of the blocks. Thus, lithium occupation of the pocket sites will more significantly remove the highly distorted NbO_6 octahedra on the edge, resulting in the disappearance of the V_{Hi} and V_{Mid} bands in the Raman spectrum.

Compared to the sites with standard E_{ads}, other sites with weaker E_{ads} are less stable and could be considered as intermediate sites in the Li diffusion pathway during the lithiation process. The kinetics of Li diffusion along the sites with lower E_{ads} was examined. The activation energy (E_{act}) of each step is detailed in Figure S9 and Table S2. The averaged E_{act} values of Li diffusion among the pocket (P), vertical (V), and horizontal (H) window sites are plotted in Figure 5d. The analysis finds that H → H diffusion (diffusion along the *b* axis) has the lowest barrier, while P → P diffusion (interdiffusion between corner-sharing blocks in the *ac* plane) has the highest barrier. Other diffusions, including V → V, V → P, and P → V inside the corner-sharing blocks, have barriers in the middle. The lowest E_{act} in H → H diffusion can be attributed to the fact that the E_{ads} values on those H sites have the smallest energetic difference (0.22 eV, Figure 4c and Table S1); on the other hand, the highest E_{act} in the P → P diffusion corresponds to the largest energetic variation between P sites (0.69 eV). E_{ads} on V sites with the intermediate variation (0.55 eV) results in diffusion barriers in the middle.

From the energetic analysis, the mechanism of lithiation at low voltage has been rationally resolved. First, Li prefers to stay at pocket sites because most of those sites have the strongest E_{ads} and their related diffusions have the highest E_{act}. Second, Li could diffuse inside the corner-sharing blocks but is less likely to interdiffuse among those blocks thorough pocket sites in edge-sharing regions. Finally, the favorable diffusion pathway is through horizontal window sites along the *b* axis due to the lowest activation barrier. Accordingly, Li ions are filled in the edge-sharing blocks and diffuse inside the 3 × 4 and 3 × 5 corner-sharing blocks, mainly through the *b* axis, during the lithiation process. The electronic structure resulting from the sequence of lithium occupation shows that electrons initially localize in the center of the blocks of H-Nb_2O_5 when the lithium is slightly adsorbed. Subsequently, more lithium adsorption on the edge-sharing NbO_6 octahedra leads to overlapped d orbitals and a progressive delocalization of electrons. This transition from electron localization to delocalization effectively explains the observed static Raman profile during the initial lithiation, while abrupt overall intensity drops occur with higher lithiation in the lower potential window. Furthermore, from a structural perspective, those filled Li ions rigidify the edge-sharing blocks and erase the Raman signals at V_{Hi} and V_{Mid}, corresponding to Nb−O stretching at edge-sharing octahedra. Thus, only the Nb−O stretching in the corner-sharing blocks (∼800 cm^{-1}) is

https://doi.org/10.1021/acsenergylett.3c01031
ACS Energy Lett. 2023, 8, 3131−3140

observed in the low-voltage range (lithiation). The results presented here, which were obtained through Raman characterization and DFT calculations, are consistent with previous studies by Koçer et al., who used nudged elastic band calculations and ab initio molecular dynamics simulations to investigate lithium diffusion in niobium tungsten oxide shear structures.[32] The study also suggests that lithium mainly diffuses through the structure by hopping between window sites in the block interior, while hops into or out of pocket sites are less frequent due to large activation energy barriers. Moreover, our findings align with those of Koçer et al., as we observed an asymmetric behavior in lithium insertion and extraction in the shear structure, which is reflected in the slightly asymmetric Raman spectrum of H-Nb_2O_5 during lithium discharge/charge processes (red zone in Figure 3a). Strong lithium adsorption energy on the pocket site and facile lithium diffusion through the window sites lead to rapid lithium transport down the tunnels and dispersal around the pocket sites, resulting in the rapid disappearance of the V_{Hi} and V_{Mid} bands in the Raman spectrum. However, the reverse process of extracting lithium from the stable pocket sites is kinetically slower, although transit from the window sites is rapid, resulting in a slightly slower recovery of the V_{Hi} and V_{Mid} bands in the Raman spectrum during the charge process. Specifically, the aforesaid anisotropic lithium pathway and asymmetric lithium (de)intercalation have several advantages. First, shear-phase materials exhibit anisotropic crystal growth down the blocks' tunnels, which is identical to the major lithium transport pathways, enabling fast lithium storage. Second, the utilization of this anisotropy during electrode preparation, such as by controlling the crystal orientation to make the 1-D channels perpendicular to the current collector, would be beneficial for decreasing tortuosity in lithium diffusion and improving the battery's charge rate, as shown for T-Nb_2O_5 with a quasi-2D lithium transport pathway.[21] This strategy could be achieved by applying an external magnetic field after introducing ferrofluid particles on the surface of the materials or by directly selecting Wadsley materials with magnetism among niobium compounds, or at least designing the ideal shear phase using dopants like Ni, Fe, and Co.[33,34] Third, the property of faster lithiation, compared to delithiation, in the shear structure makes it more suitable as an anode in a full cell. This is beneficial in meeting practical battery demands that require faster charge rates than discharge rates in portable devices and electrified vehicles.

In summary, *operando* Raman spectroscopy was utilized to investigate the changes in the vibrational bands of H-Nb_2O_5 upon lithiation. The Raman spectrum of fully lithiated H-Nb_2O_5 exhibited a decrease in the overall intensity. More specifically, the spectrum showed a vibration band at 800 cm^{-1} with a positively shifted V_{Lo} band, while the V_{Hi} and V_{Mid} bands disappeared compared to the pristine H-Nb_2O_5 spectrum. Further analysis revealed that the V_{Hi} and V_{Mid} bands correspond to the stretching modes of the shorter Nb−O bonds around the edge-sharing octahedra, while the V_{Lo} band was related to the bending modes. It was found that Li preferentially occupied the pocket site and the center of corner-sharing sites during lithiation, leading to the disappearance of the V_{Hi} and V_{Mid} bands in the Raman spectra at low voltages. The progression of orbital filling in the structure of H-Nb_2O_5 is directly linked to the sequence of the lithium occupation. At low lithium compositions, the electrons predominantly accumulate on localized, nonbonding t_{2g} orbitals of corner-shanring NbO_6 located at the center of 3 × 5 blocks, where there is no d orbital overlap with the surrounding octahedra. However, as the lithium concentration increases, it starts occupying t_{2g} levels on edge-sharing NbO_6, resulting in an increased d orbital overlap between them. This phenomenon effectively explains the origin of the abrupt and significant intensity changes observed in the *operando* Raman spectra. Moreover, energetic results demonstrated that pocket sites with the strongest E_{ads} also had the highest E_{act} for diffusions between them, making interdiffusion among those blocks through pocket sites in the edge-sharing region less likely. On the other hand, Li could diffuse inside the corner-sharing blocks, with the most favorable diffusion pathway being through horizontal window sides along the *b* axis due to their lowest activation barriers and the smallest variation of E_{ads}. This explains why only the Nb−O stretching in the corner-sharing blocks (~800 cm^{-1}) is still observed in the low-voltage range (lithiation). The integration of experimental Raman spectra and DFT calculations effectively elucidates the lithium storage mechanism of H-Nb_2O_5, including the preferred adsorption site, the related electronic structure, and the diffusion pathway of lithium. This provides fresh perspectives for comprehending the storage characteristics of other materials in the shear-phase category.

■ ASSOCIATED CONTENT

Supporting Information

The Supporting Information is available free of charge at https://pubs.acs.org/doi/10.1021/acsenergylett.3c01031.

Experimental and theoretical simulation methods, supporting figures and tables related to the characterization of materials (e.g., XRD, Raman spectra, SEM, lithium adsorption energy, and diffusion barrier), as well as discussions on the Raman intensity, and structure of H-Nb_2O_5 (PDF)

Supporting Video a: Video of computed vibrational motion (V_{Hi}) of H-Nb_2O_5 (MP4)

Supporting Video b: Video of computed vibrational motion (V_{Mid}) of H-Nb_2O_5 (MP4)

Supporting Video c: Video of computed vibrational motion of H-Nb_2O_5 around 850 cm^{-1} (MP4)

Supporting Video d: Video of computed vibrational motion (V_{Lo}) of H-Nb_2O_5 (MP4)

Supporting Video e: Video of computed vibrational motion of Li_xH-Nb_2O_5 (MP4)

■ AUTHOR INFORMATION

Corresponding Authors

Jeng-Han Wang − *Department of Chemistry, National Taiwan Normal University, Taipei 11677, Taiwan, Republic of China;* orcid.org/0000-0002-3465-4067; Email: jenghan@ntnu.edu.tw

Yabing Qi − *Energy Materials and Surface Sciences Unit (EMSSU), Okinawa Institute of Science and Technology Graduate University (OIST), Onna-son, Okinawa 904-0495, Japan;* orcid.org/0000-0002-4876-8049; Email: Yabing.Qi@OIST.jp

Meilin Liu − *School of Materials Science and Engineering, Georgia Institute of Technology, Atlanta, Georgia 30332-0245, United States;* orcid.org/0000-0002-6188-2372; Email: meilin.liu@mse.gatech.edu

https://doi.org/10.1021/acsenergylett.3c01031
ACS Energy Lett. 2023, 8, 3131−3140

Authors

Tongtong Li − *School of Materials Science and Engineering, Georgia Institute of Technology, Atlanta, Georgia 30332-0245, United States; Energy Materials and Surface Sciences Unit (EMSSU), Okinawa Institute of Science and Technology Graduate University (OIST), Onna-son, Okinawa 904-0495, Japan;* orcid.org/0000-0002-0517-2886

Shengchi Huang − *Department of Chemistry, National Taiwan Normal University, Taipei 11677, Taiwan, Republic of China*

Nicholas Kane − *School of Materials Science and Engineering, Georgia Institute of Technology, Atlanta, Georgia 30332-0245, United States*

Zheyu Luo − *School of Materials Science and Engineering, Georgia Institute of Technology, Atlanta, Georgia 30332-0245, United States;* orcid.org/0000-0002-7053-8848

Weilin Zhang − *School of Materials Science and Engineering, Georgia Institute of Technology, Atlanta, Georgia 30332-0245, United States;* orcid.org/0000-0003-2880-4492

Gyutae Nam − *School of Materials Science and Engineering, Georgia Institute of Technology, Atlanta, Georgia 30332-0245, United States*

Bote Zhao − *School of Materials Science and Engineering, Georgia Institute of Technology, Atlanta, Georgia 30332-0245, United States; School of Environment and Energy, South China University of Technology, Guangzhou 510006, People's Republic of China*

Complete contact information is available at: https://pubs.acs.org/10.1021/acsenergylett.3c01031

Author Contributions

J.-H.W. and M.L. conceived the idea. J.-H.W., Y.Q. and M. L. supervised the research. T.L. performed the experiments and analyzed the data with help from J.-H.W., N.K., Z.L., W.Z., G.N., and B.Z.. J.-H.W. and S.H. performed computational studies. All of the authors discussed the results. T.L. and J.-H.W. wrote the manuscript with input from all the authors.

Notes

The authors declare no competing financial interest.

■ ACKNOWLEDGMENTS

This work was partially supported by CBMM. The authors would like to thank Dr. Dongchang Chen and Mr. Luke Soule at Georgia Tech and Prof. Yanyan Song from Northeastern University (China) for fruitful discussions. We thank the OIST Micro/Nanofabrication Section for support. Y.Q. acknowledges support from the Energy Materials and Surface Sciences Unit of the Okinawa Institute of Science and Technology Graduate University.

■ REFERENCES

(1) Amin, R; Chiang, Y-M. Characterization of Electronic and Ionic Transport in $Li_{1-x}Ni_{0.33}Mn_{0.33}Co_{0.33}O_2$ (NMC333) and $Li_{1-x}Ni_{0.50}Mn_{0.20}Co_{0.30}O_2$ (NMC523) as a Function of Li Content [J]. *Journal of The Electrochemical Society* **2016**, *163* (8), A1512.

(2) Park, M; Zhang, X; Chung, M; Less, G B; Sastry, A M. A review of conduction phenomena in Li-ion batteries [J]. *Journal of Power Sources* **2010**, *195* (24), 7904−7929.

(3) Lu, J; Chen, Z; Ma, Z; Pan, F; Curtiss, L A; Amine, K. The role of nanotechnology in the development of battery materials for electric vehicles [J]. *Nature Nanotechnology* **2016**, *11* (12), 1031−1038.

(4) Jain, R; Lakhnot, A S; Bhimani, K; Sharma, S; Mahajani, V; Panchal, R A; Kamble, M; Han, F; Wang, C; Koratkar, N. Nanostructuring versus microstructuring in battery electrodes [J]. *Nature Reviews Materials* **2022**, *7* (9), 736−746.

(5) Griffith, K J; Seymour, I D; Hope, M A; Butala, M M; Lamontagne, L K; Preefer, M B; Koçer, C P; Henkelman, G; Morris, A J; Cliffe, M J; Dutton, S E; Grey, C P. Ionic and Electronic Conduction in $TiNb_2O_7$ [J]. *J. Am. Chem. Soc.* **2019**, *141* (42), 16706−16725.

(6) Griffith, K J; Harada, Y; Egusa, S; Ribas, R M; Monteiro, R S; Von Dreele, R B; Cheetham, A K; Cava, R J; Grey, C P; Goodenough, J B. Titanium Niobium Oxide: From Discovery to Application in Fast-Charging Lithium-Ion Batteries [J]. *Chem. Mater.* **2021**, *33* (1), 4−18.

(7) Griffith, K J; Wiaderek, K M; Cibin, G; Marbella, L E; Grey, C P. Niobium tungsten oxides for high-rate lithium-ion energy storage [J]. *Nature* **2018**, *559* (7715), 556−563.

(8) Lu, X; Jian, Z; Fang, Z; Gu, L; Hu, Y-S; Chen, W; Wang, Z; Chen, L. Atomic-scale investigation on lithium storage mechanism in $TiNb_2O_7$ [J]. *Energy & Environmental Science* **2011**, *4* (8), 2638−2644.

(9) Catti, M; Ghaani, M R. On the lithiation reaction of niobium oxide: structural and electronic properties of $Li_{1.714}Nb_2O_5$ [J]. *Phys. Chem. Chem. Phys.* **2014**, *16* (4), 1385−1392.

(10) Saber, M; Preefer, M B; Kolli, S K; Zhang, W; Laurita, G; Dunn, B; Seshadri, R; Van der Ven, A. Role of Electronic Structure in Li Ordering and Chemical Strain in the Fast Charging Wadsley−Roth Phase PNb_9O_{25} [J]. *Chem. Mater.* **2021**, *33* (19), 7755−7766.

(11) Koçer, C P; Griffith, K J; Grey, C P; Morris, A J. Cation Disorder and Lithium Insertion Mechanism of Wadsley−Roth Crystallographic Shear Phases from First Principles [J]. *J. Am. Chem. Soc.* **2019**, *141* (38), 15121−15134.

(12) Andersson, S. Arthur David Wadsley 1918 − 1969 [J]. *J. Solid State Chem.* **1970**, *1* (3), iv−vi.

(13) Cava, R J; Murphy, D W; Zahurak, S M. Lithium Insertion in Wadsley-Roth Phases Based on Niobium Oxide [J]. *Journal of The Electrochemical Society* **1983**, *130* (12), 2345.

(14) Wang, Y; Chen, D. Application of Advanced Vibrational Spectroscopy in Revealing Critical Chemical Processes and Phenomena of Electrochemical Energy Storage and Conversion [J]. *ACS Applied Materials & Interfaces* **2022**, *14* (20), 23033−23055.

(15) Lang, S; Yu, S-H; Feng, X; Krumov, M R; Abruña, H D. Understanding the lithium−sulfur battery redox reactions via operando confocal Raman microscopy [J]. *Nature Communications* **2022**, *13* (1), 4811.

(16) Hu, T; He, F; Liu, M; Chen, Y. In situ/operando regulation of the reaction activities on hetero-structured electrodes for solid oxide cells [J]. *Progress in Materials Science* **2023**, *133*, 101050.

(17) Wang, Y-H; Li, S; Zhou, R-Y; Zheng, S; Zhang, Y-J; Dong, J-C; Yang, Z-L; Pan, F; Tian, Z-Q; Li, J-F. In situ electrochemical Raman spectroscopy and ab initio molecular dynamics study of interfacial water on a single-crystal surface [J]. *Nature Protocols* **2023**, *18* (3), 883−901.

(18) Wang, Y-H; Zheng, S; Yang, W-M; Zhou, R-Y; He, Q-F; Radjenovic, P; Dong, J-C; Li, S; Zheng, J; Yang, Z-L; Attard, G; Pan, F; Tian, Z-Q; Li, J-F. In situ Raman spectroscopy reveals the structure and dissociation of interfacial water [J]. *Nature* **2021**, *600* (7887), 81−85.

(19) Zhang, J; He, W; Quast, T; Junqueira, J R C; Saddeler, S; Schulz, S; Schuhmann, W. Single-entity Electrochemistry Unveils Dynamic Transformation during Tandem Catalysis of Cu_2O and Co_3O_4 for Converting NO_3^- to NH_3 [J]. *Angewandte Chemie International Edition* **2023**, *62* (8), e202214830.

(20) Schumacher, L; Weyel, J; Hess, C. Unraveling the Active Vanadium Sites and Adsorbate Dynamics in VO_x/CeO_2 Oxidation Catalysts Using Transient IR Spectroscopy [J]. *J. Am. Chem. Soc.* **2022**, *144* (32), 14874−14887.

(21) Chen, D; Wang, J-H; Chou, T-F; Zhao, B; El-Sayed, M A; Liu, M. Unraveling the Nature of Anomalously Fast Energy Storage in T-Nb_2O_5 [J]. *J. Am. Chem. Soc.* **2017**, *139* (20), 7071−7081.

(22) Chen, D; Ding, D; Li, X; Waller, G H; Xiong, X; El-Sayed, M A; Liu, M. Probing the Charge Storage Mechanism of a

Pseudocapacitive MnO_2 Electrode Using in Operando Raman Spectroscopy [J]. *Chem. Mater.* **2015**, *27* (19), 6608−6619.
(23) Chen, D; Mahmoud, M A; Wang, J-H; Waller, G H; Zhao, B; Qu, C; El-Sayed, M A; Liu, M. Operando Investigation into Dynamic Evolution of Cathode−Electrolyte Interfaces in a Li-Ion Battery [J]. *Nano Letters* **2019**, *19* (3), 2037−2043.
(24) Wang, Y; Huang, S; Raji-Adefila, B; Outka, A; Wang, J-H; Chen, D. Unraveling the Nature and Role of Layered Cation Ordering in Cation-Disordered Rock-Salt Cathodes [J]. *J. Am. Chem. Soc.* **2022**, *144* (43), 19838−19848.
(25) Gatehouse, B; Wadsley, A. The crystal structure of the high temperature form of niobium pentoxide [J]. *Acta Crystallogr.* **1964**, *17* (12), 1545−1554.
(26) Li, T; Nam, G; Liu, K; Wang, J-H; Zhao, B; Ding, Y; Soule, L; Avdeev, M; Luo, Z; Zhang, W; Yuan, T; Jing, P; Kim, M G; Song, Y; Liu, M. A niobium oxide with a shear structure and planar defects for high-power lithium ion batteries [J]. *Energy & Environmental Science* **2022**, *15* (1), 254−264.
(27) Catti, M; Pinus, I; Knight, K. Lithium insertion properties of $Li_xTiNb_2O_7$ investigated by neutron diffraction and first-principles modelling [J]. *J. Solid State Chem.* **2015**, *229*, 19−25.
(28) Preefer, M B; Saber, M; Wei, Q; Bashian, N H; Bocarsly, J D; Zhang, W; Lee, G; Milam-Guerrero, J; Howard, E S; Vincent, R C; Melot, B C; Van der Ven, A; Seshadri, R; Dunn, B S. Multielectron Redox and Insulator-to-Metal Transition upon Lithium Insertion in the Fast-Charging, Wadsley-Roth Phase PNb_9O_{25} [J]. *Chem. Mater.* **2020**, *32* (11), 4553−4563.
(29) Kreissl, H T; Li, M M J; Peng, Y-K; Nakagawa, K; Hooper, T J N; Hanna, J V; Shepherd, A; Wu, T-S; Soo, Y-L; Tsang, S C E. Structural Studies of Bulk to Nanosize Niobium Oxides with Correlation to Their Acidity [J]. *J. Am. Chem. Soc.* **2017**, *139* (36), 12670−12680.
(30) McConnell, A A; Aderson, J S; Rao, C N R. Raman spectra of niobium oxides [J]. *Spectrochimica Acta Part A: Molecular Spectroscopy* **1976**, *32* (5), 1067−1076.
(31) Jehng, J M; Wachs, I E. Structural chemistry and Raman spectra of niobium oxides [J]. *Chem. Mater.* **1991**, *3* (1), 100−107.
(32) Koçer, C P; Griffith, K J; Grey, C P; Morris, A J. Lithium Diffusion in Niobium Tungsten Oxide Shear Structures [J]. *Chem. Mater.* **2020**, *32* (9), 3980−3989.
(33) Billaud, J; Bouville, F; Magrini, T; Villevieille, C; Studart, A R. Magnetically aligned graphite electrodes for high-rate performance Li-ion batteries [J], Nature. *Energy* **2016**, *1* (8), 16097.
(34) Erb, R M; Libanori, R; Rothfuchs, N; Studart, A R. Composites Reinforced in Three Dimensions by Using Low Magnetic Fields [J]. *Science* **2012**, *335* (6065), 199−204.

https://doi.org/10.1021/acsenergylett.3c01031
ACS Energy Lett. 2023, 8, 3131−3140